radiation. The reciprocal-lattice points $3\bar{2}3$ and $3\bar{2}0$ do not pass the Ewald sphere belonging to the wavelength of Cu $K\alpha_2$, but when the reciprocal-lattice points are replaced by spheres, these spheres touch the Ewald sphere of Cu $K\alpha_2$ and contribute to the intensity in the above-mentioned region.

Comparison of measured and calculated *Umweganregung* patterns

Fig. 2(*b*) is calculated for Cu $K\alpha_1$ radiation, Fig. 2(*c*) for Cu $K\alpha_2$ radiation. ψ is zero in the [100] direction. With these two diagrams it is possible to index all *Umweganregung* peaks of the measured pattern in Fig. 2(*a*). The indices of the operative and cooperative reflections are given in Tables 1 and 2 together with their Bragg angles and structure factors. The zero point for ψ in the measured diagram is chosen arbitrarily.

The leftmost peak in Fig. 2(*a*) is built up of the two operative reflections $2\bar{2}\bar{1}$ and $2\bar{2}4$ with Cu $K\alpha_1$ radiation. The second peak belongs to the same reflections, but for Cu $K\alpha_2$ radiation. The difference in ψ for these two peaks is $\psi_{\alpha_1} - \psi_{\alpha_2} = -0{\cdot}42°$, as can be calculated from values in Tables 1 and 2. The third peak is the peak discussed above, having a respective triangle in Fig. 2(*b*) only.

Despite the difficulty of correcting for the superposition of the Cu $K\alpha_1$ and Cu $K\alpha_2$ peaks and disregarding the problematical second peak in Table 1, one finds that the comparison of the measured and calculated intensities gives surprisingly good agreement. The disagreement between the measured and calculated intensities for the peak at $\psi = 52{\cdot}18°$ is probably due to experimental shortcomings. As can be seen in Fig. 1 the intensity ratio of the two highest peaks varies between 1 : 0·7, in good agreement with the theory, in the range 20–40° and 1 : 1 in the ψ range 50–70°, owing to inadequate measurements.

Recently Soejima, Okazaki & Matsumoto (1985) referred to a similar program for the simulation of ψ scanning.

The author is grateful to Dr G. Adiwidjaja for performing the measurements.

References

BUSING, W. R. & LEVY, H. A. (1967). *Acta Cryst.* **22**, 457–464.
COLE, H., CHAMBERS, F. W. & DUNN, H. M. (1962). *Acta Cryst.* **15**, 138–144.
POST, B. (1975). *J. Appl. Cryst.* **8**, 452–456.
POST, B. (1976). *Acta Cryst.* **A32**, 292–296.
PRAGER, P. R. (1971). *Acta Cryst.* **A27**, 563–569.
RENNINGER, M. (1937). *Z. Phys.* **106**, 141–176.
ROSSMANITH, E. (1985). *Z. Kristallogr.* **171**, 253–254.
SOEJIMA, Y., OKAZAKI, A. & MATSUMOTO, T. (1985). *Acta Cryst.* **A41**, 128–133.
ZACHARIASEN, W. H. (1965). *Acta Cryst.* **18**, 705–710.

Acta Cryst. (1986). **A42**, 348–352

Experimental Observation of the Borrmann Pyramid – the Borrmann Fan for Four-Beam Transmission of X-rays*

BY CÍCERO CAMPOS

Instituto de Física, Universidade Estadual de Campinas, Campinas, SP 13100, *Brazil*

AND SHIH-LIN CHANG†

Instituto de Física, Universidade Estadual de Campinas, Campinas, SP 13100, *Brazil, and Department of Physics, National Tsing Hua University, Hsinchu, Taiwan* 300

(*Received* 16 *October* 1985; *accepted* 1 *April* 1986)

Abstract

The polyhedron which confines the Poynting vectors of *N*-beam transmissions in crystal space is referred to as the Borrmann pyramid. The observation of this Borrmann pyramid is realized from the diffraction images of the four-beam, (000)(220)($2\bar{2}0$)(400), transmission case of silicon single crystals for Mo $K\alpha$. The directions of the Poynting vectors for the eight modes of wave propagation involved and the diffraction images are calculated. These calculations confirm the experimental observations. The variation of the direction of the Poynting vector for each mode is also reported.

* This work forms part of the PhD dissertation of CC.
† Present address: National Tsing Hua University.

0108-7673/86/050348-05$01.50 © 1986 International Union of Crystallography

I. Introduction

Transmission(Laue)-type multiple diffraction has long been studied for investigating the dynamical interaction of wavefields in crystals, in particular, the enhanced anomalous transmission effect of Borrmann & Hartwig (1965). Since 1965, there have been several articles on the theoretical and experimental aspects of this diffraction phenomenon. These include the work of Saccocio & Zajac (1965*a*, *b*), Hildebrandt (1967), Joko & Fukuhara (1967), Ewald & Heno (1968), Heno & Ewald (1968), Uebach & Hildebrandt (1969), Balter, Feldman & Post (1971), Umeno & Hildebrandt (1975), Post, Chang & Huang (1977), Høier & Aanestad (1981), and many others. Fairly complete references are given by Chang (1984). Most of these deal with anomalous transmission in thick crystals. Only a limited number are concerned with thin crystals. In such cases other dynamical effects, like *Pendellösung* [see Hart & Lang (1961), Høier & Aanestad (1981)], were often the main goal of the investigation.

In this article, we investigate the Borrmann-fan effect in N-beam transmission cases for thin crystals. The N-beam Borrmann fan, which forms a polyhedron in crystal space, is called, hereafter, the Borrmann pyramid. The formation of the Borrmann pyramid, though not unexpected, has not been studied in the light of the dynamical theory of X-ray diffraction. For this purpose, investigations, both experimental and theoretical, have been carried out and the results are reported here.

II. Theoretical considerations

The Ewald dynamical theory (Ewald, 1916, 1917), in Laue's formulation (von Laue, 1931), for N-beam transmission is adopted here. The fundamental equation of wavefields is treated as an eigenvalue equation. Since the dielectric constant of the crystal is complex, the eigenvalues are also complex. The real parts of the eigenvalues specify the coordinates of the tie points (Ewald, 1916) on the dispersion surface. The imaginary parts are proportional to the linear absorption coefficients. Each eigenvalue defines a type of wave propagation for the wave field inside the crystal, a so-called mode of propagation. Usually, the number of modes in an N-beam transmission diffraction is $2N$, where the factor of 2 is due to the two polarized components, σ and π, of the wave field.

The eigenvectors yield the amplitude ratios among the diffracted waves, $D_0 : D_H : D_P : D_Q : \ldots$. The subscripts indicate the involved waves 0, H, P and Q, the 0 wave being the incident wave. The magnitudes of the wave fields are then determined by the boundary conditions for wave fields at the entrance and exit surfaces, *i.e.* the continuity of the tangential components of the electric fields and the continuity of the normal components of the electric displacements. The Poynting vector for a given mode j inside the crystal then takes the form (for example, see Kato, 1974)

$$\mathbf{S}_j(\mathbf{r}) = (c/8\pi) \sum_H \hat{\mathbf{K}}_H |D_H(j)|^2 \times \exp[-4\pi k\delta''(j)\hat{\mathbf{n}}_e \cdot (\mathbf{r}-\mathbf{r}_e)], \qquad (1)$$

where δ'' is the imaginary part of the accommodation δ (Ewald, 1916), the eigenvalue for mode j. $D_H(j)$ is the electric displacement of mode j for the reflection H. The unit vector $\hat{\mathbf{n}}_e$ is the inward surface normal to the entrance surface. $\mathbf{K}_H$ and $\mathbf{k}_H$ are the wave vectors inside and outside the crystal for the H reflection. The magnitude k is equal to $1/\lambda$. $\hat{\mathbf{K}}_H$ is the unit vector of $\mathbf{K}_H$. The vector $\mathbf{r}_e$ is the position vector of the entrance surface.

As is well known in two-beam diffraction, the Borrmann fan is the area spanned by the Poynting vectors within the crystal. The direction of the Poynting vector lies in the plane of incidence for the given reflection.

In a multi-beam case, the Poynting vectors span in three-dimensional space. The direction of energy flow for each mode of propagation should be defined by at least two angles. In addition, the Poynting vector is perpendicular to the dispersion surface (Kato, 1958). Calculation for the coordinates of tie points on the dispersion surface should be carried out so as to determine the direction of Poynting vectors.

III. Calculations

The calculation procedure given by Chang (1984) is employed. Since the calculation of the present case involves the dispersion surface in reciprocal space and the direction of Poynting vectors in real space, the coordinates chosen for the reciprocal and the real space are shown in Figs. 1(*a*) and (*b*) respectively. The four-beam, (000)(220)($2\bar{2}0$)(400), case of silicon for Mo $K\alpha$ is considered here. In Fig. 1(*a*), the Laue point L is chosen as the origin for the coordinates x, y, z. The x direction is perpendicular to the crystal plate, which is parallel to the (001) planes. The yz plane is parallel to the crystal plate. The z axis is chosen to be perpendicular to the reciprocal-lattice vector **0P** of the 400 reflection. **0H** and **0Q** are the reciprocal-lattice vectors of the (220) and ($2\bar{2}0$) planes. C is the center of the circle circumscribing the four reciprocal-lattice points 0, H, P and Q. The coordinates of an entrance point $A(x, y, z)$ are defined by the azimuthal angle ψ and the angular deviation $\Delta\theta$ from the exact Bragg angle θ_p of the 400 reflection:

$$x = (\Delta\theta)k \sin\psi \sin\theta_p, \qquad y = (\Delta\theta)k \cos\psi,$$
$$z = (\Delta\theta)k \sin\psi \cos\theta_P. \qquad (2)$$

T is a tie point for a mode of propagation, AT is the accommodation equal to $k\delta$ (Ewald, 1916) and is perpendicular to the entrance surface. In Fig. 1(b), the origin of the coordinate system in real space is the point at which the incident beam impinges on the entrance surface of the crystal. The axes x, y and z have the same meaning as those of Fig. 1(a). The Poynting vector $\mathbf{S}_j$ of mode j is defined by the polar angle θ_j and the azimuthal ψ_j. Points 0, H, P and Q are the points of interception of the diffracted beams 0, H, P and Q with the exit surface of the crystal. The polyhedron $E0HPQ$, formed by the Borrmann fans of the reflections H, P, Q, $H-P$ and $P-Q$, is the expected Borrmann pyramid.

Fig. 2 is the intersection of the dispersion surface with the xy plane, which shows the dispersion curves along the 400 reflection line. There are eight curves for the eight modes. The corresponding linear absorption coefficients are plotted in Fig. 3. At the exact four-beam point, $ZZ = 0$, modes 1 and 2 are the lowest absorbing modes, having their dispersion sheets closest to the Laue point.

The directions of the Poynting vectors for the eight modes involved are then determined by calculating the angles θ_j and ψ_j for the normals to the corresponding dispersion sheets at various tie points. Fig. 4 shows the interception of the Poynting vectors with the plane $0HPQ$ in reciprocal space. This is obtained at the angular deviation $\Delta\theta = 2''$ and the azimuth ψ varying from 0 to 360° in increments of 4°. The coordinate and absicissa are defined as

$$X_w = k \sin\theta_p - k\cos\theta_p \tan\theta_j \sin\psi_j$$
$$Y_w = k\cos\theta_p \tan\theta_j \cos\psi_j. \qquad (3)$$

To prevent confusion, the pair of modes that have almost the same dispersion curves (see Fig. 2) are

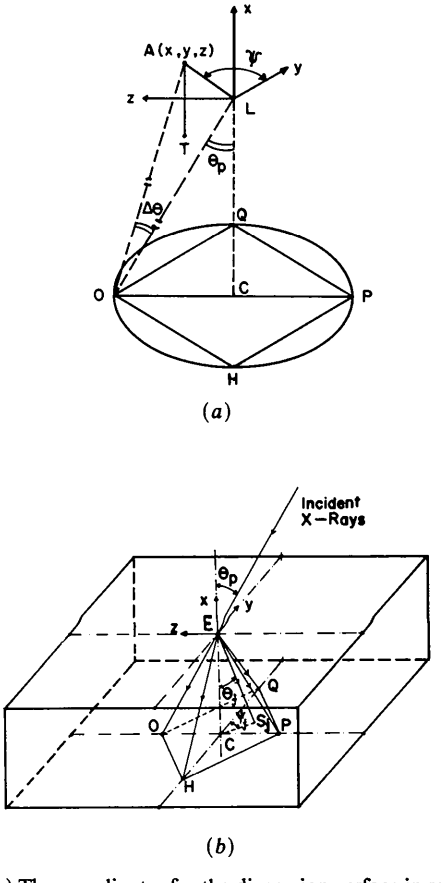

Fig. 1. (a) The coordinates for the dispersion surface in reciprocal space; (b) the coordinates in crystal space used to define the direction of the Poynting vector $\mathbf{S}_j$.

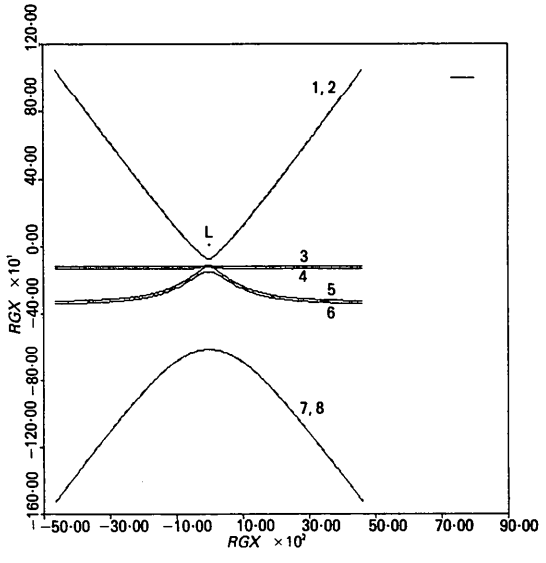

Fig. 2. Calculated dispersion curves along the 400 reflection line. The coordinate and abscissa are the x and z axes of Fig. 1(a). The scale is cm^{-1}. The position with $x = z = 0$ is the Laue point (L).

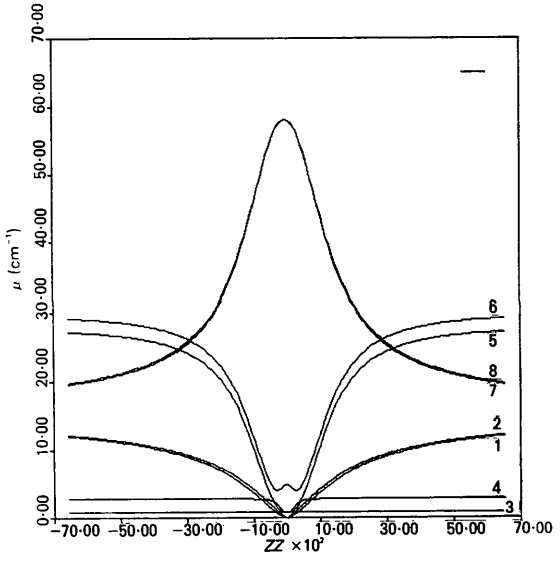

Fig. 3. Calculated linear absorption coefficients for Fig. 2. The abscissa ZZ is the z axis of Fig. 1(a). The scale of ZZ is cm^{-1}.

represented by a single curve for their Poynting vectors in Fig. 4. The distribution of points along these curves shows the distribution of the Poynting vectors in reciprocal space, *i.e.* the distribution of rays in real space. Comparison between this diagram and Fig. 2 can be made by considering the normals of the dispersion curves in Fig. 2 and tracing them along the *HQ* direction in Fig. 4.

From Fig. 4, one observes that modes 1 and 2 have the same distribution of rays as modes 7 and 8, except that the latter has a shorter circumference. The distribution of modes 3 and 4 resembles that of modes 5 and 6. However, the former is confined within the area circumscribed by the curve of modes 7 and 8.

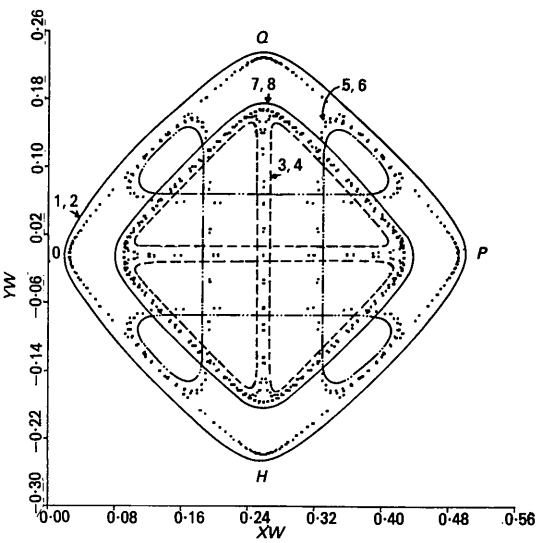

Fig. 4. The interception (points) of the Poynting vectors of the eight modes with the plane $0HPQ$ of Fig. 1(*b*) for $\Delta\theta = 2''$. The solid and broken lines serve as guides for the eye. The coordinates are defined in equation (3). The scale is Å^{-1}.

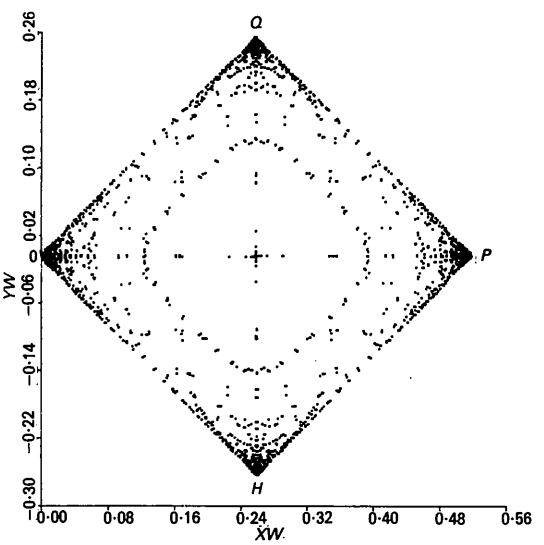

Fig. 5. The distribution of the Poynting vectors of Fig. 4 for $\Delta\theta$ varying from 0 to 20″.

Fig. 5 is the superposed distribution of the Poynting vectors of Fig. 4, calculated for $\Delta\theta$ ranging from 0 to 20″ with the increment 0·1′. All the Poynting vectors lie inside the square $0HPQ$. The center of the square corresponds to the position of the exact four-beam point. Hot corners are seen. This is very similar to the hot-edge effect in two-beam diffraction for a very thin crystal, *i.e.* $\mu t \sim 1$ (Kato, 1974). At the center of the square the density of the Poynting vectors is higher than the densities around the center. Overlapping of the points is expected. Calculations have also been performed for $\Delta\theta$ greater than 20″. However, none of the Poynting vectors lies outside the square. This provides the evidence that all the Poynting vectors are confined in the Borrmann pyramid $E0HPQ$. Consequently, for a weakly or nonabsorbing crystal with respect to the wavelength used, all the diffracted beams should have diffraction images in the form of a square. These images should, in principle, be observable.

IV. Experimental

The experimental set-up sketched in Fig. 6 was used to observe the square-formed images. It consisted of a Rigaku microfocus X-ray generator (Microflex) and a Lang topographic camera. In order to vary the crystal thickness at will, wedge-shaped perfect silicon crystals were used as the samples. The entrance crystal surface is a [001]-cut face. The exit crystal surface made an angle of 20° with the entrance surface. The direction of the thickness gradient is along the [010] direction. The slit for blocking the direct beam was so placed that part of the image of the directly diffracted beam could be observed.

The sample was aligned for 400 reflection for Mo $K\alpha$ (Fig. 6*b*). The beam size was about 2 cm high and 100 μm wide. Topographs were then taken in the usual way. Figs. 7(*a*), (*b*) and (*c*) are the section topographs for μt equal to 2, 6 and 10, respectively. The normal absorption coefficient is $14{\cdot}4\ \text{cm}^{-1}$. The left line is the image of the direct beam. The image of the *Pendellösung* of the 400 reflection is on the right. The transmitted reflection images of the 220

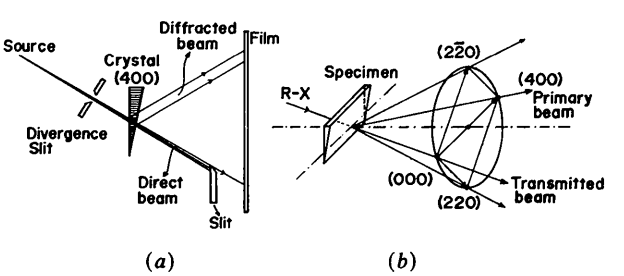

Fig. 6. (*a*) A schematic representation of the experimental set-up; (*b*) geometric relationship among the diffracted beams.

and $2\bar{2}0$ reflections are shown in the middle of the figures. For the thin crystal, $\mu t \sim 2$ (Fig. 7*a*), the approximately rectangular images of the four-beam Borrmann fans, both Mo $K\alpha_1$ and Mo $K\alpha_2$, are clearly seen for the [220] and [$2\bar{2}0$] reflected directions. The shapes of the Borrmann fans which are not square are due to the inclination of the exit crystal surface with respect to the entrance surface. The images are therefore the projection of the square $0HPQ$ on the exit surface. When the crystal thickness is increased by lowering the sample with respect to the incident beam, the images of the direct beams still exhibit the sharp edges of the Borrmann fans, while the images of the 220 and $2\bar{2}0$ become slightly blurred (Fig. 7*b*). For the very thick crystal, $\mu t \sim 10$, the images of the fans were reduced to the lines shown in Fig. 7(*c*). The enhanced anomalous transmission for the direct beam is clearly seen. This thickness dependence of the diffraction images is very similar to that often encountered in two-beam dynamical diffractions, except that the absorption of the effective modes, *i.e.* modes 1 and 2, is much lower than the minimum value $\mu = 0{\cdot}8$ cm^{-1} in two-beam 400 reflection (see Fig. 2).

V. Discussion

From the calculation and the experimental results obtained, we have demonstrated that the multi-beam Borrmann fan is the result of the formation of a Borrmann pyramid by the Poynting vectors within the crystal. For the images of the Borrmann fan to be observed, a thin crystal, with $\mu t < 2$, should be used. It has also been shown that the Poynting vectors for a given N-beam case should lie inside the Borrmann pyramid. The variation in directions of the Poynting vectors inside the crystal depends on the propagation of the wave fields, *i.e.* the mode of wave propagation. In this study we have presented the spatial distribution of the Poynting vectors for each mode of propagation. This calculation therefore provides a direct insight to the relation between the energy flow and the modes of wave propagation in N-beam diffractions.

The authors are indebted to the CNPq (Conselho Nacional de Pesquisa e Tecnologia) and TELEBRÁS (Telecomunicacão do Brasil) for financial support. One of us (CC) is grateful to the FAPESP (Fundacão Amparo de Pesquisa do Estado de São Paulo) for providing a graduate fellowship.

References

BALTER, S., FELDMAN, R. & POST, B. (1971). *Phys. Rev. Lett.* **27**, 307–309.
BORRMANN, G. & HARTWIG, W. (1965). *Z. Kristallogr.* **121**, 401–409.
CHANG, S. L. (1984). *Multiple Diffraction of X-rays in Crystals.* Heidelberg: Springer-Verlag.
EWALD, P. P. (1916). *Ann. Phys. (Leipzig)*, **49**, 1–38, 117–143.
EWALD, P. P. (1917). *Ann. Phys. (Leipzig)*, **54**, 519–597.
EWALD, P. P. & HENO, Y. (1968). *Acta Cryst.* A**24**, 5–15.
HART, M. & LANG, A. R. (1961). *Phys. Rev. Lett.* **7**, 120–121.
HENO, Y. & EWALD, P. P. (1968). *Acta Cryst.* A**24**, 16–24.
HILDEBRANDT, G. (1967). *Phys. Status Solidi*, **24**, 245–261.
HØIER, R. & AANESTAD (1981). *Acta Cryst.* A**37**, 787–794.
JOKO, T. & FUKUHARA, A. (1967). *J. Phys. Soc. Jpn*, **22**, 597–604.
KATO, N. (1958). *Acta Cryst.* **11**, 885–886.
KATO, N. (1974). In *X-ray Diffraction*, edited by L. V. AZAROFF, pp. 263–295. New York: McGraw-Hill.
LAUE, M. VON (1931). *Ergeb. Exacten Naturwiss.* **10**, 133–158.
POST, B., CHANG, S. L. & HUANG, T. C. (1977). *Acta Cryst.* A**33**, 90–97.
SACCOCIO, E. J. & ZAJAC, A. (1965*a*). *Acta Cryst.* **18**, 478–480.
SACCOCIO, E. J. & ZAJAC, A. (1965*b*). *Phys. Rev. A*, **139**, 255–264.
UEBACH, W. & HILDEBRANDT, G. (1969). *Z. Kristallogr.* **129**, 1–8.
UMENO, M. & HILDEBRANDT, G. (1975). *Phys. Status Solidi A*, **31**, 583–594.

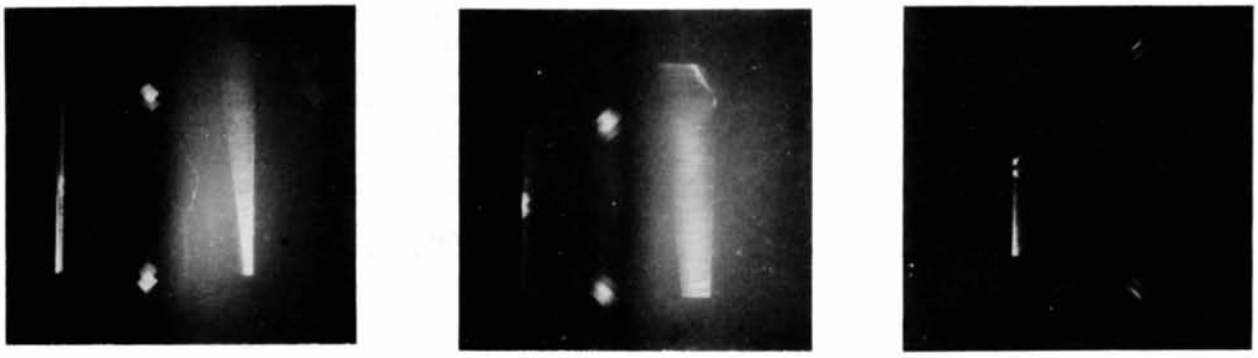

(*a*) (*b*) (*c*)

Fig. 7. Section topographs of the four-beam case for (*a*) $\mu t \sim 2$, (*b*) $\mu t \sim 6$ and (*c*) $\mu t \sim 10$. The experimental conditions are 40 kV and 0·4 mA. The exposure times are 5, 6, and 3 h for (*a*), (*b*) and (*c*), respectively.